PNAS
www.pnas.org

Supplementary Information for

Ab Initio Spectroscopy and Ionic Conductivity of Water at Earth Mantle Conditions

Viktor Rozsa, Ding Pan, Federico Giberti, Giulia Galli

Giulia Galli
E-mail: gagalli@uchicago.edu

This PDF file includes:

Supporting Information Text

Simulation Conditions. The pressure and temperature conditions considered in our simulations are reported in Table S1, together with computed diffusion coefficients.

Ionic species and Ionic Lifetimes. We analyzed the presence of ionic species in compressed water as a function of time for the ~11 and ~20 GPa trajectories (see Table S1). Ionic species were defined using criteria based on hydrogen bonding analysis. We defined a hydrogen and an oxygen atom as hydrogen bonded when the distance between them is less than the second minimum of the OH radial distribution function (RDF) and the deviation of the O – H...O angle from a straight line is $< 30^{\circ}$(1). Here O – H denotes a covalent bond and H...O an hydrogen bond. Using this definition, we constructed the hydrogen bond network of each snapshot of our trajectories, and then mapped the network onto a graph, with oxygens as vertexes and hydrogen bonds as direct connections between pairs of vertexes.

In this framework, a hydronium ion, composed of three hydrogens and a central oxygen, was identified as a chemical species donating three hydrogen bonds to its vicinal neighbors. A hydroxide ion, composed of one hydrogen and one oxygen, was identified as a chemical species donating one hydrogen bond while accepting three or more hydrogen bonds. This strategy has also been used to identify constituent ions in water at ambient conditions (2).

The variation of the number of hydronium and hydroxide species over two short trajectories at 11 and 20 GPa is plotted in Fig. S1, where the number of the two species has been represented in different quadrants for clarity. The formation of H_3O^+ and OH^- is clearly correlated, indicating that dissociation occurs as a bimolecular process. Fig. S1 shows a larger concentration of hydroxide and hydronium ions at 20 than at 11 GPa; the same trend was found over the entire trajectory.

We also investigated whether "free hydrogens" were present in our simulations. For each hydrogen, at each step we calculated its coordination number with respect to oxygen. A hydrogen was considered "free" if its coordination was 0, i.e. no oxygen was present within a distance equal to the first minimum of the OH RDF. Then, for each free hydrogen, we counted the number of contiguous snapshots over which the hydrogen persists as a free species. We defined the lifetime, τ, of the free hydrogen as the time an hydrogen atom spends as a free species. We constructed an histogram of all computed τ. By normalizing the histogram with respect to the total number of snapshots and total number of hydrogens, we obtained the probability, at a given time step, to observe a free hydrogen with a lifetime τ. Fig. S2 displays the computed probabilities for two choices of cutoff distances for a 3 ps portion of the 20 GPa trajectory containing dissociation events. We found extremely small values of τ (<0.3 fs) with very low probabilities ($< 2\text{x}10^{-5}$). Hence our results show that free hydrogens are fleeting species, with no evidence of long-lived free hydrogens arising from unimolecular dissociation.

Ionic Conductivity. We computed the ionic conductivity within linear response, using the Green-Kubo formalism. Instead of directly evaluating the integral of the correlation function of the total dipole moment derivative, we employed the Einstein relation:

$$\sigma = \lim_{t\to\infty} \frac{1}{6tk_bTV}\langle[\vec{M}(t) - \vec{M}(0)]^2\rangle \qquad [1]$$

Where k_b is Boltzmann's constant, T is the temperature, V is the cell volume, and the angled brackets indicate the average over time origins.

In order to minimize statistical errors in the evaluation of eq. 1, we partitioned the trajectories over which $\vec{M}(t)$ was computed into many separate portions of length 10 ps. The results are shown in Fig. S3, where we also display the time progression of the average. As reported in the main text, we obtain $\sigma \sim 1$ $(\Omega\text{cm})^{-1}$ at 11 $\pm$1 GPa, 1000 K, and $\sigma \sim 10$ $(\Omega\text{cm})^{-1}$ at 20 $\pm$1 GPa, 1000 K. We note that the values of the conductivity computed over the 10 ps segments exhibited a standard deviation of the mean of 0.3 $(\Omega\text{cm})^{-1}$ at 11 GPa, 1000 K, and 1.0 $(\Omega\text{cm})^{-1}$ at 20 GPa, 1000 K. A comparison of the averages over partitions at both conditions is presented in Fig. S4, clearly displaying the higher conductivity of the water at 20 GPa.

Our estimates of σ are compared to other experimental (3, 4) and computational (5, 6) studies on the conductivity of water along the principal Hugoniot in Fig. S5. In Table S2 we also present the data corresponding to Fig. S5, including temperatures. While temperatures were not reported in Refs. (4) and (6), we obtained temperatures in both cases from closely related publications by the same authors.

Raman Spectra.

Polarizability. Within density functional perturbation theory(7), the μth Cartesian component P^μ of the polarization of a macroscopic sample is given by:

$$P^\mu = -\frac{4e}{V}\sum_{n=1}^{N}\langle\Delta^{\mathbf{E}}\psi_n|\bar{\psi}_n^\mu\rangle \qquad [2]$$

where $\mathbf{E}$ is a perturbing electric field and $\Delta^{\mathbf{E}}\psi_n$ is the response of the nth Kohn-Sham eigenfunction of the unperturbed Hamiltonian, $\hat{H}$, under the influence of $\mathbf{E}$. $\Delta^{\mathbf{E}}\psi_n$ and $\bar{\psi}_n^\mu$ are computed by solving two linear systems subsequently:

$$(\hat{H} - \epsilon_n)|\bar{\psi}_n^{\mu}\rangle = P_c[\hat{H}, \mathrm{r}^{\mu}]|\psi_n\rangle, \quad [3]$$

$$(\hat{H} - \epsilon_n)|\Delta^{\mathbf{E}}\psi_n\rangle = -e\sum_{\mu} \mathrm{E}^{\mu}|\bar{\psi}_n^{\mu}\rangle - P_c\Delta V^{lf}|\psi_n\rangle, \quad [4]$$

where $\mathbf{r}$ is the position operator, ϵ_n and ψ_n are the nth eigenvalue and eigenvector of the unperturbed Hamiltonian, and n belongs to the valence band; $P_c = 1 - \sum_n |\psi_n\rangle\langle\psi_n|$ is a projector operator (n runs over all occupied states), ΔV^{lf} is the change of the local potential arising from the change in charge density $n(\mathbf{r})$: $\Delta^{\mathbf{E}} n(\mathbf{r}) = 4\sum_{n=1}^{N} \psi_n^{\star}(\mathbf{r})\Delta^{\mathbf{E}}\psi_n(\mathbf{r})$. In our calculations, an electric field is applied along each Cartesian axis and the elements of the polarizability tensor α are obtained by dividing the corresponding component of the polarization by the electric field strength.

Isotropic, Anisotropic, and Unpolarized Raman. Isotropic and anisotropic Raman spectra are defined as:

$$R_{\mathrm{iso}}(\omega) \propto \frac{\hbar\omega}{k_b T}\int dt e^{-i\omega t}\langle\bar{\alpha}(0)\bar{\alpha}(t)\rangle \quad [5]$$

$$R_{\mathrm{aniso}}(\omega) \propto \frac{\hbar\omega}{k_b T}\int dt e^{-i\omega t}\langle\frac{2}{15}\mathrm{Tr}\beta(0)\beta(t)\rangle \quad [6]$$

In equations 5 and 6, ω is the frequency, Tr is the trace, and $\bar{\alpha}$ and β are the isotropic and anisotropic components of the polarizability tensor, α: $\bar{\alpha} = \frac{1}{3}\mathrm{Tr}\alpha$ and $\beta = \alpha - \bar{\alpha}\mathbf{I}$, where $\mathbf{I}$ is the identity tensor. Unpolarized Raman spectra are computed as $R_{\mathrm{unpol}} = R_{\mathrm{iso}} + \frac{7}{4R_{\mathrm{aniso}}}$ (8).

Intermolecular and Intramolecular Decomposition. In a periodic system, the ground state maximally localized Wannier functions (MLWF), w_n, may be obtained by applying a unitary transformation $\mathbf{u}$ to the eigenstates of the Kohn-Sham Hamiltonian: $w_n = \sum u_{mn}\psi_m$. By applying the same unitary transformation to $\Delta^E\psi$ and $\bar{\psi}$, we obtain the response wavefunctions $\Delta^{\mathbf{E}}w_n$ and $\bar{w_n}$, corresponding to each of the MLWFs. By replacing $\Delta^{\mathbf{E}}\psi_n$ and $\bar{\psi_n}$ in eq. 2 with $\Delta^{\mathbf{E}}w_n$ and $\bar{w_n}$, we obtain the projection of the total polarization onto the nth MWLF:

$$P_{w_n}^{\mu} = -\frac{4e}{V}\langle\Delta^{\mathbf{E}}w_n|\bar{w}_n^{\mu}\rangle \quad [7]$$

We then define the effective polarizability of each MLWF as:

$$\mathbf{P}_{w_n} = \alpha_{w_n}^{\mathrm{eff}}\mathbf{E} \quad [8]$$

There are four MLWFs associated with each intact water molecule, corresponding to two covalent bonds pairs (BP), and two lone pairs (LP). The effective molecular polarizability of the ith water molecule is:

$$\alpha_i^{\mathrm{eff}} = \alpha_{i,\mathrm{BP1}}^{\mathrm{eff}} + \alpha_{i,\mathrm{BP2}}^{\mathrm{eff}} + \alpha_{i,\mathrm{LP1}}^{\mathrm{eff}} + \alpha_{i,\mathrm{LP2}}^{\mathrm{eff}} \quad [9]$$

The total system polarizability, α, is the sum over all α_i^{eff}. We cast the expression of the Raman intensities (eq. 5, 6) in terms of effective molecular polarizability:

$$R_{\mathrm{iso}}(\omega) \propto \frac{\hbar\omega}{k_b T}\int dt e^{-i\omega t}\langle\sum_{i,j}\bar{\alpha}_i^{\mathrm{eff}}(0)\bar{\alpha}_j^{\mathrm{eff}}(t)\rangle \quad [10]$$

$$R_{\mathrm{aniso}}(\omega) \propto \frac{\hbar\omega}{k_b T}\int dt e^{-i\omega t}\langle\frac{2}{15}\mathrm{Tr}\sum_{i,j}\beta_i^{\mathrm{eff}}(0)\beta_j^{\mathrm{eff}}(t)\rangle \quad [11]$$

Where $\bar{\alpha}^{\mathrm{eff}} = \frac{1}{3}\mathrm{Tr}\alpha^{\mathrm{eff}}$ and $\beta^{\mathrm{eff}} = \alpha^{\mathrm{eff}} - \bar{\alpha}^{\mathrm{eff}}\mathbf{I}$, and $\mathbf{I}$ is the identity tensor. Tr denotes the trace operator. By separating $i = j$ and $i \neq j$ terms of the summation, we obtain the intramolecular and intermolecular contributions to the Raman intensity, respectively.

Infrared Spectra. Due to the highly dissociative nature of water considered in our simulations, molecular dipole moments may not be well defined. Hence, we expressed the infrared spectra intensity, $A(\omega)$ in terms of the time derivative of the sample dipole moment (9):

$$\begin{aligned} A(\omega) &\propto \frac{2\pi\omega^2\beta}{3cV}\int dt e^{-i\omega t}\langle\vec{M}(0)\vec{M}(t)\rangle \\ &= \frac{2\pi\beta}{3cV}\int dt e^{-i\omega t}\langle\dot{\vec{M}}(0)\dot{\vec{M}}(t)\rangle \end{aligned} \quad [12]$$

Where $\vec{M}(t)$ is defined as:

$$\vec{M}(t) = e\cdot\sum_{i=1}^{N_H}\vec{R}_i^H(t) + 6e\cdot\sum_{i=1}^{N_O}\vec{R}_i^O(t) - 2e\cdot\sum_{i=1}^{N_{MLWF}}\vec{R}_i^{MLWF}(t) \quad [13]$$

as in the discussion of ionic conductivity in the main text; e is the elementary charge, $\vec{R}^O(t)$ and $\vec{R}^H(t)$ are the coordinates of oxygen and hydrogen atoms, respectively, and $\vec{R}^{MLWF}(t)$ are the coordinates of the center of a maximally localized Wannier function. The summations run over all species of the simulation cell. Time derivatives of $\vec{M}(t)$ were computed using finite differences.

The correlation function in eq. 12 is classical, requiring a quantum correction factor to approximate the quantum time correlation function (10). Here we used the so-called harmonic prefactor, which has been shown to satisfy the fluctuation-dissipation theorem and detailed balance (11).

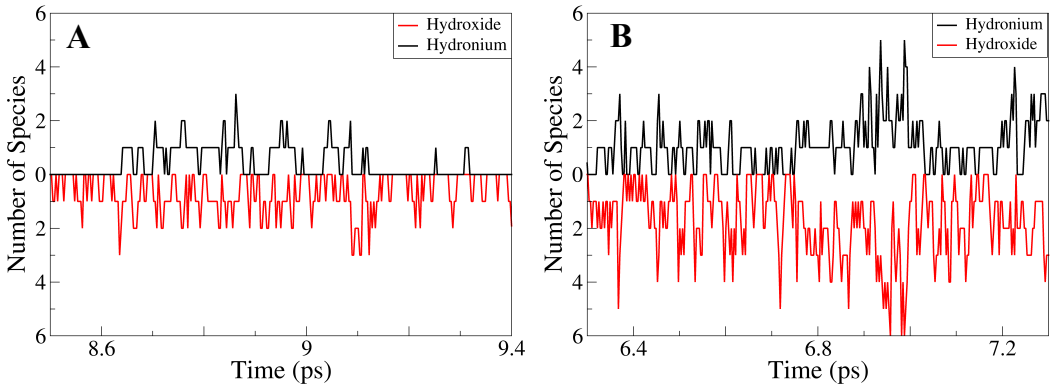

Fig. S1. Number of ionic species along a short 11 (A) and 20 (B) GPa trajectory (see text for definition of hydronium and hydroxide ions).

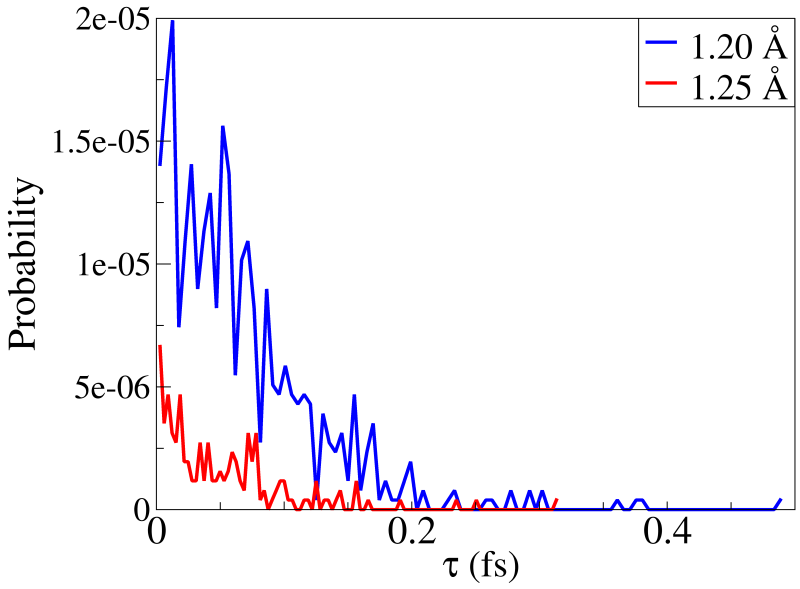

Fig. S2. Probability to observe a free hydrogen as a function of lifetime τ (see text for definition) over a 3 ps trajectory at 20 GPa, 1000 K. We show results for two cutoff distances: 1.25 Å, corresponding to the first minimum of the O-H RDF, and a cutoff 4% percent smaller.

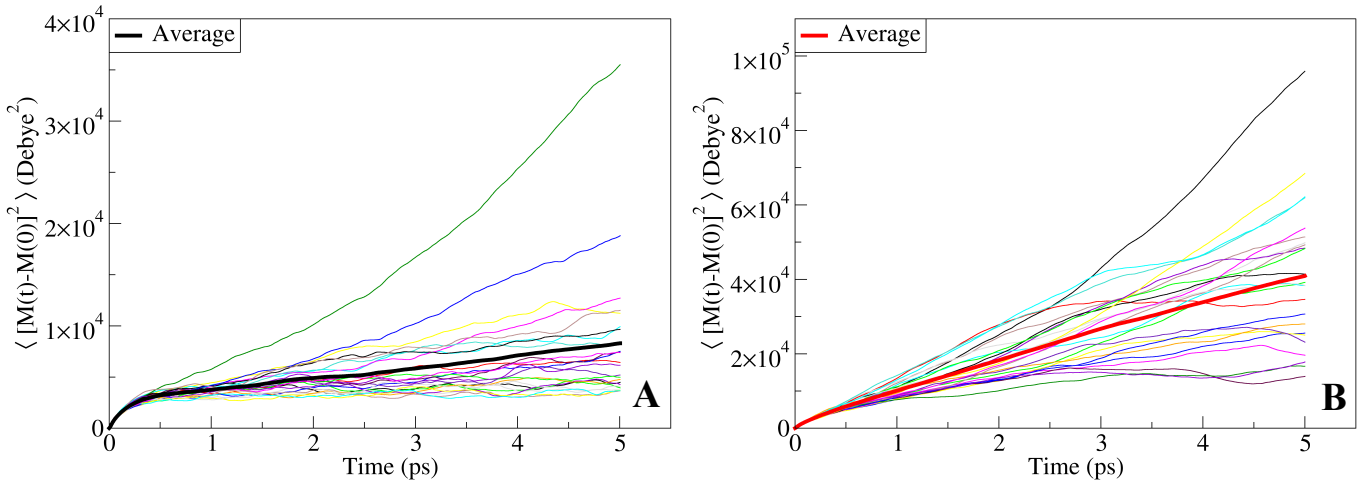

Fig. S3. Time-averaged mean squared displacement of the total dipole moment $\vec{M}$ as a function of separation time for multiple partitioned segments of length 10 ps from a 240 ps trajectory at 11 GPa and 1000K (A) and 20 GPa and 1000 K (B). The average over segments for 11 GPa and 1000 K is reported as a thick black curve, yielding $\sigma \sim 1$ $(\Omega\text{cm})^{-1}$. Similarly, the average over segments for 20 GPa and 1000 K is reported as a thick red curve, yielding $\sigma \sim 10$ $(\Omega\text{cm})^{-1}$.

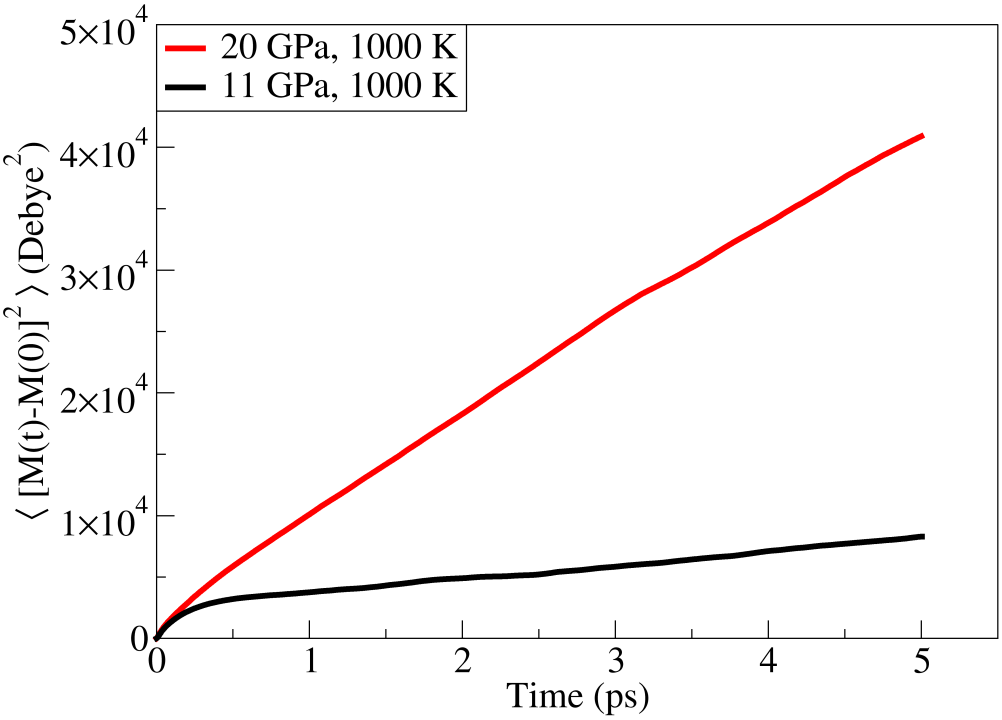

Fig. S4. Comparison of the averages of time-averaged mean squared displacement of the total dipole moment $\vec{M}$ as a function of separation time for multiple partitioned segments of length 10 ps at 11 GPa and 1000 K and 20 GPa and 1000 K. The average over segments for 11 GPa, 1000 K is reported as a black curve ($\sigma \sim 1$ $(\Omega\text{cm})^{-1}$) while the average over segments for 20 GPa, 1000 K is reported as a red curve ($\sigma \sim 10$ $(\Omega\text{cm})^{-1}$)

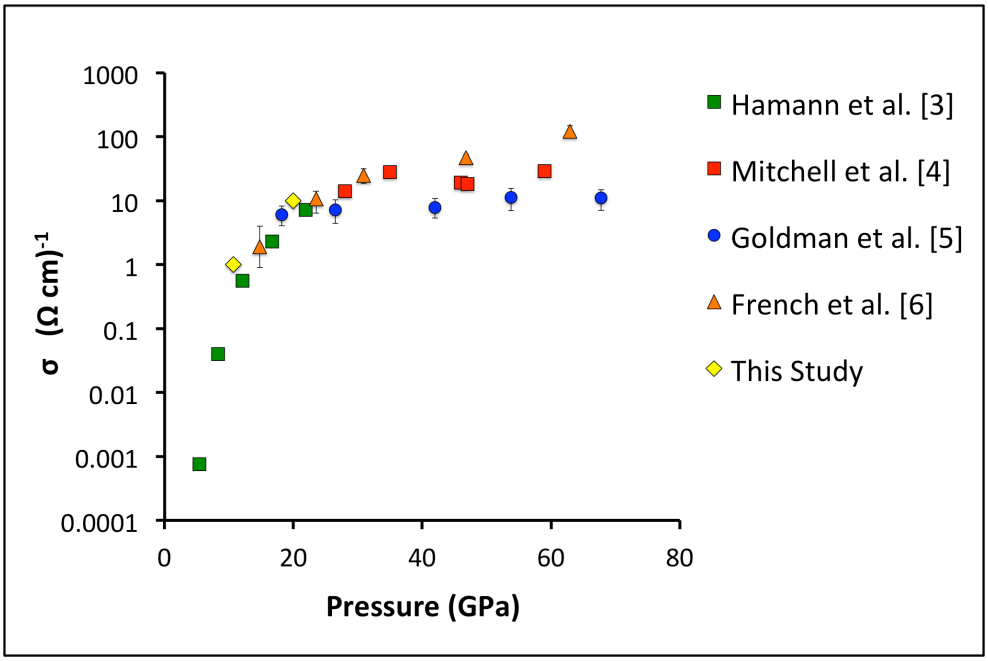

Fig. S5. The ionic conductivities of water as a function of pressure, along the principal Hugoniot. Hamann et al. (3) and Mitchell et al. (4) reported experimental shock studies. Goldman et al. (5) reported a computational study of shocked water, using Mulliken charges, and French et al. (6) reported a computational study using diffusion coefficients of free protons. Temperatures for all data points are presented in Table S2.

Table S1. Density (ρ), computed temperature (T), pressure (P) and oxygen (D_O) and hydrogen (D_H) diffusion coefficients for three first principles molecular dynamics trajectories. Averages were computed over 240 ps.

ρ (g/cm^3)	T (K)	P (GPa)	D_O (cm^2/sec)	D_H(cm^2/sec)
1.57	1020 $\pm$ 50	11 $\pm$ 1	~9x10^{-5}	~9x10^{-5}
1.86	1020 $\pm$ 51	20 $\pm$ 1	~3x10^{-5}	~7x10^{-5}
1.86	510 $\pm$ 25	16 $\pm$ 1	nondiffusive	nondiffusive

Table S2. Pressure (P), temperature (T), and conductivity (σ) of water along the principal Hugoniot, as displayed in Fig. 4. Temperatures for Mitchell et al. (4) were obtained from the same group's later study, reported in Ref. (12). Temperatures for French et al. (6) were obtained from the same group's earlier study, reported in Ref. (13).

Study	P (GPa)	T (K)	σ $((\Omega\text{cm})^{-1})$
Hamann et al. (3)	5.4	547	0.00076
	8.3	731	0.04
	12.1	991	0.56
	16.7	1326	2.3
	21.9	1710	7.1
Mitchell et al. (4)	28.0	1790	14
	35.0	2200	28
	46.0	3030	19
	47.0	3090	18
	59.0	3810	29
Goldman et al. (5)	18.2 ± 0.2	791 ± 7	6.0 ± 2
	26.5 ± 0.4	1167 ± 4	7.2 ± 3
	42.0 ± 0.3	1995 ± 8	7.9 ± 3
	53.8 ± 0.3	2744 ± 10	11.2 ± 4
	67.8 ± 0.2	3654 ± 6	11.1 ± 4
French et al. (6)	14.8	1010	2 ± 1
	23.5	1550	11 ± 4
	30.9	2000	25 ± 7
	46.8	3010	47 ± 10
	62.9	4040	122 ± 26
This study	11 ± 1	1020 ± 50	~ 1
	20 ± 1	1020 ± 51	~ 10

References

1. Luzar A, Chandler D (1996) Hydrogen-bond kinetics in liquid water. *Nature.* 379:55.
2. Giberti F, Hassanali A (2017) The excess proton at the air-water interface: The role of instantaneous liquid interfaces. *J. Chem. Phys.* 146:244703.
3. Hamann S, Linton M (1966) Electrical conductivity of water in shock compression. *Trans. Faraday Soc.* 62:2234.
4. Mitchell A, Nellis W (1982) Equation of state and electrical conductivity of water and ammonia shocked to the 100 gpa (1 mbar) pressure range. *J. Chem. Phys.* 76:6273.
5. Goldman N, et al. (2009) Ab initio simulation of the equation of state and kinetics of shocked water. *J. Chem. Phys.* 130:124517.
6. French M, Mattsson T, Redmer R (2010) Diffusion and electrical conductivity in water at ultrahigh pressures. *Phys. Rev. B.* 82:174108.
7. Baroni S, Gironcoli SD, Corso AD, Giannozzi P (2001) Phonons and related crystal properties from density-functional perturbation theory. *Rev. Mod. Phys.* 73:515.
8. Long D (2002) *The Raman Effect: A Unified Treatment of the Theory of Raman Scattering by Molecules.* (John Wiley and Sons, New York).
9. Thomas M, Brehm M, Fligg R, Vohringer P, Kirschner B (2013) Computing vibrational spectra from ab initio molecular dynamics. *Phys. Chem. Chem. Phys.* 15:6608.
10. Bader J, Berne B (1994) Quantum and classical relaxation rates from classical simulations. *J. Chem. Phys.* 100:8359.
11. Ramierez R, Lopez-Ciudad T, Kumar P, Marx D (2004) Quantum corrections to classical time-correlation functions: hydrogen bonding and anharmonic floppy modes. *J. Chem. Phys.* 121:3973.
12. Lyzenga G, Ahrens TJ, Nellis WJ, Mitchell AC (1982) The temperature of shock-compressed water. *J. Chem. Phys.* 76:6282–6286.
13. French M, Redmer R (2009) Estimating the quantum effects from molecular vibrations of water under high pressures and temperatures. *J. Phys. Condens. Mat.* 21:6059.